

One-step plasma synthesis of Nb₂O₅ nanofibers and their enhanced photocatalytic activity

Dr. Shin Kajita*[†]

Mr. Fumiaki Mimuro [‡]; Prof. Tomoko Yoshida [§]; Prof. Noriyasu Ohno [†]

Dr. Naoaki Yoshida [¶]

1 Abstract

Fiberform nanostructured niobium (Nb) was fabricated by one step helium (He) plasma irradiation. He ion implantation formed He nano-bubbles on a Nb plate and led to formation of protrusions while migrating in Nb matrix; fiberform nanostructures (FN) were grown when the fluence became high ($>10^{26}$ m⁻²). The necessary conditions for the formation of Nb FN were revealed to be the surface temperature range of 900-1100 K and the incident ion energy higher than 70 eV. The sample was oxidized at 573-773 K in an air atmosphere, and Pt nanoparticles were photo-deposited on the Nb₂O₅ samples. The surface was analyzed by scanning electron microscope, transmission electron microscope, x-ray photoelectron spectroscopy, and ultraviolet-visible spectrophotometry. Photocatalytic activity of the fabricated materials was studied using methylene blue (MB) decolorization process. An enhanced photocatalytic performance was identified on FN Nb₂O₅ substrate with Pt deposition.

2 Introduction

Niobium (Nb) pentaoxide (Nb₂O₅) is popular semiconductor because of its stability and various applications: gas sensor [1], solar energy conversion [2, 3],

*corresponding author

[†]Institute of Materials and Systems for Sustainability, Nagoya University, Nagoya 464-8603, Japan

[‡]Graduate School of Engineering, Nagoya University, Furo-cho, Chikusa, Nagoya 464-8603, Japan

[§]The Osaka City University Advanced Research Institute for Natural Science and Technology, Sumiyoshi, Sugimoto-cho, 3-3-138, Osaka 558-8585, Japan

[¶]Research Institute for Applied Mechanics, Kyushu University, Kasuga, Fukuoka 816-8580, Japan

lithium ion battery [4], catalysts [5], and photocatalysts [6, 7]. Concerning photocatalysis application, after the discovery of hydrogen (H_2) production from water splitting using titanium oxide (TiO_2) by Honda and Fujishima [8], development of highly effective photocatalysts has been extensively explored [9, 10]. Nb_2O_5 is one of the candidate materials for heterogeneous photocatalysts to split water [11, 12, 13], degradation of organic compounds in water and air [7], and other various processes [14, 15]. Enhanced photocatalytic performances were identified on various nanosized Nb_2O_5 materials including C, N co-modified niobium pentoxide nanoneedles [16] and core-shell nanocomposites [17]. Because highly porous materials are thought to enhance the activity of photocatalysis [2, 18], many works have been reported about fabrication of mesoporous Nb_2O_5 nanostructures via such as sol-gel process [19], electrospinning [15], evaporation induced self-assembly method [11, 13], and solvothermal reaction [6].

Recently, Novakowski *et al.* reported that helium (He) ion beam can be used for one-step fabrication of Nb_2O_5 nanostructures [3]; nanometer sized protrusion were formed on the surface by He ion irradiation. Effects of He plasma irradiation on metals have been investigated widely during the last decade. Fiberform nanostructures (FNs), called fuzz, were found to be formed on tungsten (W) by He plasma irradiation [20]. Later on, formation of FN was identified on various metals [21, 22, 23, 24, 25, 26]. It was found that FN was easily formed on high shear modulus materials such as W, molybdenum [22], rhodium, rhenium, and ruthenium [26], while they were difficult to be formed on low shear modulus metals [26, 27]. Since Nb has a rather low shear modulus (~ 32 GPa [28]), it is likely that FN is not easily formed. Indeed, Novakowski *et al.* and Omori *et al.* reported formations of pinholes and protrusions rather than FN [3, 24]. Photocatalytic/photoelectrochemical application using He plasma treated surfaces have been explored using W oxides [29, 30, 31], iron oxides [32, 33], titanium oxides [34], and vanadium oxides [35]. Enhanced photocatalytic performances were identified on those He treated materials probably because of increased surface area. However, it was also found that the presence of impurities, various oxides phases, and damages formed by He ion implantation could lead to degradations of photocatalytic performance.

In this paper, we will further investigate He irradiation effects on Nb to fabricate highly porous Nb (and Nb oxides) FN by He plasma irradiation. In the latter half of this study, as focusing on the application to photocatalysis, we will investigate the photocatalytic performance of the fabricated Nb_2O_5 FN. In addition to mesoporous nanostructures, it is known that the combination with loading of nanoparticulate cocatalysts significantly improves photocatalytic property [36]; photodeposition of Pt nanoparticles is conducted on the fabricated FN after oxidation to Nb_2O_5 . The photocatalytic activity is assessed using methylene blue (MB) decolorization. An enhanced photocatalytic activity is shown on Pt loaded FN Nb_2O_5 sample, and the potential mechanism is discussed.

3 Experimental

3.1 Plasma irradiation

0.1 mm thick Nb (Nilaco. Co.) samples were exposed to He plasmas in the linear shaped plasma device NAGDIS-II (Nagoya divertor simulator-II) [37]. The plasma was produced between a LaB₆ cathode heated with a carbon heater and a copper anode, and the plasma was diffused from a hole on the anode. The plasma streamed to a downstream region along with a magnetic field line, whose strength was ~ 0.1 T. Typically, the plasma density and the temperature were $< 10^{19} \text{ m}^{-3}$ and ~ 5 eV. Because the He gas pressure during the plasma irradiation was 5-10 mTorr, which was much higher than the background gas pressure (on the order of 10^{-7} Torr), interaction between He ions and a substrate is the dominant process. Morphology changes by the He plasma irradiation was known to be controlled by two important parameters [38]: the surface temperature and the incident ion energy. The surface temperature was measured by a radiation pyrometer (KTL-PRO, Lec Co. Ltd.) at the wavelength of 1.6 μm ; the emissivity of 0.22 was used for the measurement [39]. The incident ion energy was controlled by biasing the sample negatively in the plasma and determined by the potential difference from the space potential of the plasma, which was measured with an electrostatic probe.

The sample was equipped on a cooling stage to control the temperature. The sample temperature was determined by the heat flux from the plasma and thermal diffusion to the cooling stage. Thus, it was difficult to control He flux and T_s at the same time, because thermal resistance is rather uncontrollable. The irradiation experiments were conducted with changing the incident ion energy, the He flux, and the irradiation time.

3.2 Post-irradiation preparation

Using FN samples fabricated in the previous section, samples for photocatalytic experiments were prepared, as summarized in Table 1. Nb1-4 corresponds to pristine Nb samples; the surface of Nb1 was oxidized at room temperature (RT), and Nb2-4 were oxidized samples in a furnace at 573, 673, and 773 K, respectively, for 1h at air atmosphere. In addition to the oxidized samples, platinum (Pt) nanoparticles were photo-deposited [40] on oxidized Nb samples. Flat surface and FN samples oxidized at 773 K for an hour, i.e. Nb4 and FN4, were submerged in an aqueous methanol solution containing K₂PtCl₆ and irradiated with UV light. The amount of K₂PtCl₆ was chosen so that Pt content became 1.0wt% as measuring the mass of the sample. After three hours UV irradiation, the sample was rinsed with distilled water, and then, the sample was dried in a furnace at 323 K for 12 hours. Pt deposited Nb4 and FN4 samples are called Nb5 and FN5, respectively, hereafter, as shown in Table 1.

3.3 Sample characterization

The fabricated samples are characterized by scanning electron microscope (SEM) and transmission electron microscope (TEM), X-ray photoelectron spectroscopy (XPS), X-ray diffraction (XRD), and ultraviolet-visible spectrophotometry (UV-Vis). For reflectance measurement, the measurement was conducted using a UV-Vis spectrophotometer (UV-2600, Shimadzu Co. Ltd.). In addition, thermal desorption spectroscopy (TDS) was used to investigate the behavior of He atoms existed inside materials. The TDS system measures the pressures of gases using a quadrupole mass analyzer with increasing the sample temperature in a controlled manner in a high vacuum. The pressures can be converted to desorbed numbers of atoms from the sample after calibration, though we did not conduct the calibration, because the purpose of the analysis was qualitative understanding of the temperature dependence of He mobility.

3.4 Methylene blue decolorization

Photocatalytic activity of the fabricated samples was measured using MB decolorization process. The MB ($C_{16}H_{18}ClN_3S$) is an organic matter often used to measure the photocatalytic activity from the absorption spectrum of its aqueous solution. It was pointed out that the MB was not appropriate to assess the photocatalytic performance for visible-light responsive photocatalysts [41]. In the present study, we used an optical filter to cut out the visible light and checked UV response only. A prepared sample ($5 \times 5 \text{ mm}^2$) was placed in 2.5 ml of aqueous MB solution ($10 \mu\text{mol/l}$). UV light from 300 W Xenon lamp irradiates samples through an UV transmission optical filter (UTVAF-33U, Sigmakoki Co. Ltd.), whose transmission wavelength is in the range of 250-390 nm. Also, a cooling fan was used not to heat up the solution during the UV irradiation. The light transmission of aqueous MB solution was measured using the spectrophotometer, and the absorption peak intensity at 664 nm was used to measure the absorbance. The relative concentration of MB, which was the concentration normalized to the initial value, was deduced using the time course of the absorbance. Before starting the UV irradiation, the sample was placed in the MB solution for more than 10 hours to saturate the surface absorption.

4 Plasma synthesis of FN Nb

4.1 Morphology changes

Figures 1(a-c) show SEM micrographs of Nb surfaces exposed to He plasmas at different surface temperatures, T_s , i.e., 1000, 1400, and 1510 K, respectively. The incident ion energy, E_i , was 76 eV and the He ion fluence, Φ_{He} , was in the range of $8.6\text{-}13 \times 10^{25} \text{ m}^{-2}$. The irradiation time was 1 hour. The influence of the difference in the He fluence here was minor compared with the temperature dependence, and the He fluence dependence will be discussed next. Pinholes are identified on the surfaces in Fig. 1(b,c). The size of pinhole likely reflects

that of He bubble formed by the He implantation [42]. The size of the pinholes increased with the temperature; the trend was also identified on other metals such as W and Ta [42]. Pinholes were formed even at 1000 K; the size of pinholes was much smaller and protrusions were more prominent in Fig. 1(a). The morphology changes were identified on the entire surface. Different from W case, where grain orientation dependence with grain boundary was identified [43], there were no clear grain boundary and grain orientation dependence.

Figure 2 presents a He fluence dependence of the morphology change. The surface temperature was in the range of 1000-1100 K and the incident ion energy was 76-82 eV. The irradiation times of Fig. 2(a-c) were 1, 3, and 10 h, respectively. Differences in the incident ion energy and the surface temperature had only a minor influence here. Also, the difference in the ion flux by $\sim 20\%$ ($2.4 - 3.1 \times 10^{22} \text{ m}^{-2}$) had a minor effect, considering the fact the irradiation time was changed by a factor of three or greater. Initially identified protrusion were developed to FNs when the irradiation time became 3 h. No clear difference was identified between the 3 h and 10 h samples from the top view. We also observed the cross section of FN layers both on 3h and 10h irradiated Nb samples; the thickness of the FN layer was almost the same on both samples. The features of the FNs were similar to those observed on other metals including W. The required Φ_{He} for FN growth was one order of magnitude more than W cases, which required Φ_{He} of $1-3 \times 10^{25} \text{ m}^{-2}$ [38]. In previous studies, though protrusions were formed on Nb, no FNs were identified on the surface [3, 24]; this would be because of the difference in the He flux and fluence. The He flux in this study was typically $3 \times 10^{22} \text{ m}^{-2}\text{s}^{-1}$, which was more than one order of magnitude greater than previous studies. Thus, although the irradiation time of 3 hours was shorter than the previous studies (4-5 hours), the total fluence was much greater.

Figures 3(a,b) show TEM micrographs of an FN sample at different magnifications. The irradiation condition of the sample was as follows: T_s was 1100 K, E_i was 82 eV, and Φ_{He} was $\sim 4 \times 10^{26} \text{ m}^{-2}$. The sample was prepared by a focused ion beam (FIB) milling after the surface was coated with a carbon ink to support the FNs even after the FIB process. Many He bubbles were observed inside the fibers, as shown in Fig. 3(b). In addition to large He bubbles 20-30 nm in diameter, which could be easily identified, smaller nm sized bubbles were also found. FNs were formed on the layer with large (several hundred nm) cavities; the thickness of the FN layer was $\sim 1 \mu\text{m}$ and the width of fibers was typically less than 100 nm. The polygonal shaped cavities are significantly grown He bubbles. Similar large cavities were previously identified on other metals such as titanium (Ti) and W surfaces after He plasma irradiation [44, 45]. On Ti case, only nano-cones without FNs were formed on the surface by He plasma irradiation presumably due to sputtering. In the energy range of 70-100 eV, the sputtering yield of Nb by He bombardment is $2-4 \times 10^{-3}$ [46], which is one order of magnitude less than that for Ti [47]. Thus, the difference in the sputtering yield could have led to the difference in the morphology changes (nanocones for Ti and FNs for Nb). Figure 3(d) shows a color mapping of Nb (green) and oxygen (red) of the structure shown in Fig. 3(c). On this sample, no ink coating

was conducted. The green colored Nb structure was covered with red colored oxide layer, the thickness of which was ~ 5 nm. As was discussed previously [48], the surface was easily oxidized naturally at room temperature.

Figure 4 summarizes the relationship between the irradiation condition (T_s and E_i) and morphology changes. The irradiations time was 1h (flat, pinholes, protrusions) or 3h (FNs). Morphology changes can be categorized to no changes (flat), pinholes, protrusions, and FNs. No significant changes occurred when T_s was less than 900 K, and only pinholes were identified when T_s was higher than 1200 K. Protrusions were formed when T_s was in between 900-1200 K. We confirmed that FNs could be formed when T_s was 960-1120 K, $E_i > 70$ eV, and the irradiation time was 3h. The FN formation condition in T_s and E_i is overlapped with the protrusion formed condition and likely almost the same as those for protrusions except for the irradiation time (or Φ_{He}). High fluence irradiation, typically 3h irradiation, changed to FN from the protrusion.

4.2 Discussion

Figure 5 shows a TDS spectrum of a sample with FNs. The irradiation condition of the sample was as follows: E_i was 82 eV, T_s was 1100 K, and Φ_{He} was $4.1 \times 10^{26} \text{ m}^{-2}$. TDS analysis is helpful to understand the general behavior of He atoms during the irradiation in Nb regardless of morphology. In addition to the spectrum, temperature windows for three typical morphology changes, i.e., FN, protrusion, pinhole, are presented in Fig. 5. TDS spectrum had a desorption peak around 400-800 K and another peak at 1400 K. The temperature regions for the protrusions and FNs were in between the two peaks, and the tendency was consistent with other metals [49, 44]. In general, migration of interstitial atoms or released atoms from clusters or bubbles becomes active with increasing the material temperature, and gas desorption occurs when migration of atoms is enhanced. The lower temperature peak suggested that the He migration, which is necessary to form He clusters and bubbles, became significant around the temperature. The higher peak suggested that the He migration became too much, and most of the He atoms were desorbed. The upper axis represents the surface temperature normalized to the melting point, T_m , of 2750 K. The range of T_s/T_m for the protrusion formation was 0.32-0.45. It was summarized in a previous study that the formation condition of FNs was in the range of $0.25 < T_s/T_m < 0.6$ [26]; the temperature range for Nb FN growth was consistent with other metals.

As was discussed in the previous section, the sputtering yield of Nb by He ions was $2\text{-}4 \times 10^{-3}$ in the energy range of 70-100 eV, and the formed FN layer was $\sim 1.5 \mu\text{m}$. For W cases [50], when the incident ion energy was 200-300 eV and the sputtering yield was $2\text{-}5 \times 10^{-3}$, the thickness of W FN layer was 2.5-8 μm . Since the thickness of FN layer is proportional to the square root of time without erosion, the saturation thickness l_{FN} with erosion can be written as [50]

$$l_{\text{FN}} = D/E, \quad (1)$$

where D is a coefficient for the diffusion process for the FN growth [51] and E is the erosion rate. Thus, the fact that the thickness of saturation layer was $1.5 \mu\text{m}$ suggested that the growth rate of FN on Nb was 2-5 times less than W case.

He plasma irradiation has been conducted on various metals and Fig. 6 summarized how easily the FN formation occurred on the metals in terms of the shear modulus and the melting point. Note that the shear modulus is thought to be an important parameter for the FN formation [52, 21]. In Fig. 6, averaged shear modulus values between $0.25T_m$ and $0.5T_m$ with error bars, representing the minimum and maximum values in the temperature region, were plotted considering the temperature dependences. In Fig. 6, recently reported He irradiation effects on vanadium (V) [35] and Nb in this study were added to the previous summary [26], as using the temperature dependences of shear modulus for V and Nb [28]. FN growth occurred easily on metals whose shear modulus was high ($> 100 \text{ GPa}$) and the melting point was high ($> 2000 \text{ K}$). Also, no FN growth occurred on metals whose shear modulus is low ($< 30 - 40 \text{ GPa}$) and the melting point is low ($< 1500 \text{ K}$). The melting point of Nb is rather high (2750 K), but the shear modulus is low (32 GPa [28]). At the moment, the shear modulus of Nb is likely the lowest among the metals where FN was formed by He plasma irradiation, suggesting that the melting point is also an important factor for the FN growth. It might have been easier for high melting point metals to find the appropriate temperature window experimentally. As demonstrated in [33], He irradiation to metals deposited on glass substrate will be necessary for photocatalytic application. Considering thin films deposited on glass substrate, it is also necessary to take into account the softening point of the substrate. In the present study, it took three hours to make FN surfaces. Three hours could be too long from a practical point of view. A recent study revealed that metallic particle precipitation accelerated the FN growth by 100-100000 times for W and molybdenum [53]. Thus, based on the necessary conditions revealed in this study, it is of interest to seek optimized conditions with additional Nb precipitation for practical application; Nb FN may also be grown much shorter time.

The colors of the FN and pinhole samples were visually black and silver, respectively, though it had a metallic luster before the irradiation. Apparently, the optical property was altered by the morphology change. Figure 7 shows the wavelength dependence of the reflectance of the pristine, pinhole, and FN samples together with a handbook value [54]. Here, the reflectance includes both the specular and diffuse reflectance. The reflectance of the flat sample was 40-60%, while it decreased to $\sim 30\%$ for the pinhole sample, and that of the FN sample was $\sim 15\%$. Because the FN increases the optical absorbance significantly, the FN surface could be appropriate for solar-thermal application [3], similar to W cases [55]. Although the oxide layer was formed on the surface, because the thickness was likely thin (several nm), the reflectance should correspond to that of the bulk metal in Fig. 7. When it comes to photocatalytic application, because it is necessary to measure the absorbance of the oxidized layer, the reflectance shown in Fig. 7 does not necessarily influence the photocatalytic activity directly. The variation in absorbance after oxidation will be

discussed later. Another important factor for photocatalysts is the surface area [56]. Previously, the Brunauer-Emmett-Teller (BET) method was applied to W FN surface formed by He plasma irradiation [57]. The surface area increased with the FN layer thickness and was ~ 20 times greater than flat surface when the thickness of FN layer was $1 \mu\text{m}$. Since the specific surface area is orders of magnitudes smaller than powdered samples, BET analysis is not easy for plate samples. On W samples, the BET measurement was conducted using many samples to reach the detection limit. However, it is not easy to conduct the BET measurement for Nb FN samples, because fuzzy structures are more difficult to be fabricated compared with W. From the analogy to W case, the surface area of FN Nb samples would be more than 10 times greater than a flat sample when FN was formed on the surface.

5 Photocatalytic application

5.1 Sample characterizations

Figures 8(a-c) represent the SEM micrographs of Nb2-4, respectively. Although no changes were identified on Nb2 and Nb3 samples, the surface was roughed on Nb4. Because the sample broke apart when the temperature was higher than 773 K, we could not increase the temperature further. It is likely that oxidation progressed quicker and to deeper region at 773 K or higher temperatures compared with lower temperature cases. That could lead to form cracks and rough surfaces at 773 K. FN1-FN4 are FN samples oxidized at RT, 573, 673, and 773 K, respectively, in the same way as of Nb1-4. Figure 8(d) shows the SEM micrograph of FN4, suggesting that FNs remained even after the oxidation. Although SEM micrographs of FN1-3 are not shown here, Fig. 8(d) suggested that morphology changes from non-oxidized sample was also minor for FN1-3.

Figures 8(e,f) show TEM micrographs of Pt-FN sample. Even after the above deposition procedures, the FN was preserved, as shown in Fig. 8(e). The number of He bubble decreased and the size of He bubble was enlarged. Many black dots, which represent Pt nanoparticles, can be identified on the surface. Typical size of Pt particles was $\sim 1 \text{ nm}$, and the surface was covered with Pt particles.

Fabricated samples were analyzed by XPS. XPS analysis was chosen because it is sensitive to the top surface layer. Figures 9(a,b) show XPS Nb 3d spectra of Nb1-Nb5 and FN1-FN5, respectively, after calibrating the binding energy (BE) using the O 1s peak at 530.5 eV [58]. Two peaks at ~ 207.0 and 210.0 eV correspond to Nb $3d_{5/2}$ and Nb $3d_{3/2}$, respectively. As summarized previously [58], the BEs of Nb, NbO, NbO₂, and Nb₂O₅ are 202.3, 204.6, 205.5, and 207.3 eV, respectively, with an ambiguity of 0.2-0.5 eV; one can say that Nb₂O₅ was formed on all the samples including the sample oxidized at RT. On Nb1 and FN1, a small peak was identified around 202 eV, which corresponds to Nb $3d_{5/2}$ peak for Nb, indicating that the thickness of oxidized layer was thin ($< 10 \text{ nm}$).

Pt 4f peaks observed on Nb5 and FN5 were shown in Fig. 9. A mixture

of three different states of Pt were found on these samples. Rather than Pt⁰⁺ (71.7 and 75.2 eV) peak, Pt²⁺ (72.7 and 76.6 eV) and Pt⁴⁺ (74.1 and 78.0 eV) [59] peaks were stronger especially on Nb5 sample. The results suggested that the photo-deposited Pt was not sufficiently reduced to Pt⁰⁺. Dominant states of Pt on Nb5 were Pt²⁺ and Pt⁴⁺, while Pt⁰⁺ also exists on FN5; the reduction of Pt was proceeded more on FN5 compared to Nb5. It is generally recognized that Pt⁰⁺ contributes to the separation of electron-hole pairs, and recombination centers of those pairs can be formed when the concentration of Pt²⁺ and Pt⁴⁺ is too high [13]. Thus, the difference may lead to the degradation of the photocatalytic performance on Nb5 surface, which will be shown next.

5.2 A case study: methylene blue decolorization

Figure 10(a) shows a schematic of the experimental setup. Figure 10(b) shows the time courses of MB concentration during UV light irradiation on Nb1-4 and FN1-4 samples together with no sample case (control). The rate of the MB decolorization with samples was faster than that the controlled case and increased with the oxidation temperature. The highest rate was identified on Nb4 and FN4, which were oxidized at 773 K. However, no significant difference was found between the flat and FN samples. Although the effective surface area of FN samples should be sufficiently greater than flat samples, the results suggested that the nanostructure did not enhance the photocatalytic activity.

The same MB decolorization experiments were conducted using Pt deposited samples, i.e. Nb5 and FN5. Figure 11 shows the time courses of MB concentration during UV light irradiation on Nb5 and FN5 together with Nb4 and no sample case. It should be noted that we cannot quantitatively compare between Figs. 10(b) and 11, because the UV irradiation power was slightly altered. The decolorization rates of Nb5 and FN5 were higher than Nb4, indicating that the Pt loading enhanced the photocatalytic reactivity. Moreover, the decolorization rate of FN5 was higher than that of Nb5. The enhancement of the photocatalytic efficiency was better for FN samples after Pt loading. Dotted lines in Fig. 11 represent the time course of the MB concentration in the second time using the same sample to ensure the recycle performance of these catalysts. Both of the samples exhibited almost the same performance, indicating a high recycle performance of Nb₂O₅, as was reported [7]. Here, because the recycling experiments showed that Nb5 and FN5 were stable, it was likely that as-formed sample FN4 was also stable. In future, it is necessary to investigate further recycle experiments.

5.3 Discussion

It is known that the photocatalytic efficiency of Nb₂O₅ is limited by its high recombination rate of photo-induced hole-electron pairs [13]. Mesoporous structures could be one solution to increase the efficiency [11]. Different from well-known mesoporous structures such as mesoporous silica and alumina, where pores are aligned beautifully in the whole structures, He bubbles existed only

inside the FN and the pores were covered by the surface layers. However, in addition to the inside pores, previous fractal analysis using gas absorption revealed that surface fractality of a thin ($\sim 1 \mu\text{m}$) FN layer W sample was higher than 2.8 in mesoporous scale [60], indicating that surface was also really rough. Despite that fact, the photocatalytic activities were comparable between Nb1-4 and FN1-4 samples. In other words, considering the fact that the effective surface area of FN samples were higher than Nb samples, the He plasma irradiation degraded the photocatalytic activity per surface area. Similar phenomenon was previously observed on the photocatalytic efficiency of cone shaped TiO_2 surfaces formed by He plasma irradiation [34]. Although the efficiency was improved by nano-cone formation, the enhancement was sufficiently less than the enhancement in the surface area. Similarly, on He plasma treated hematite, the increase in the photocurrent was much lower than that in the active surface area [32]. It was discussed that presences of defects and impurities lead to those degradation.

Figure 12 shows XRD patterns of oxidized Nb samples at 773 K before and after He plasma irradiation. Comparing with known peaks of Nb_2O_5 [61], notable peaks were (100) and (110) peaks for oxidized Nb sample without He plasma irradiation, while (001) peak appeared after He plasma irradiation; no clear impurities were identified in the XRD pattern. Considering the fact that a decrease in (100) peak and the new (110) peak appeared after He plasma irradiation, it can be said that the crystallinity was altered by the He plasma irradiation. Because the XRD analysis is not sensitive to the surface thin layer, the variation in the top surface layer less than 100 nm is likely to be greater. As was previously identified on W [62], He implantation could perturbed atomic arrangement in the top surface layer ($< 10 \text{ nm}$). Similarly, the existence of He bubbles and clusters might have deteriorated the crystallinity of Nb_2O_5 and balanced out the increase in the effective surface area.

The photocatalytic efficiency was improved on Pt deposited Nb_2O_5 samples, i.e., Nb5 and FN5, and the improvement was better for the FN sample. It was likely that the cocatalyst suppressed the recombination of formed hole-electron pairs. Figure 13(a) shows diffuse reflectance spectra of Nb4, Nb5, FN4, and FN5. We applied here the following Kubelka-Munk transformation

$$F(R_\infty) = \frac{(1 - R_\infty)^2}{2R_\infty} \quad (2)$$

assuming that the oxidized layer is sufficiently thick and the influence of the bulk metal can be neglected [63]. The absorbance increased on all the four samples in the wavelength range less than 400 nm. Comparing between with and without Pt photo-deposition, Pt photo-deposition increased the absorbance less than 400 nm in both flat and FN samples. When the surface has a FN layer, absorption increased significantly in the UV range. Moreover, absorption in a wider wavelength range, which can be seen when local surface plasma resonance occurs [64], was identified on FN5 and slightly on Nb5. The results suggested that UV light could be efficiently absorbed on the Pt deposited FN sample, and they contributed to the electron-hole pair formation, which lead to the

enhancement in the photocatalytic activity. Figure 13(b,c) shows Kubelka-Munk plots of Nb4,5 and FN4,5, respectively. The band gap energies were deduced to be ~ 3.2 eV for Nb4,5 and FN4 samples and 3.4 eV for FN5 sample. The band gap energy of FN5 is consistent with that identified on Nb₂O₅ of 3.4 eV [7].

From the TEM micrograph of FN5 sample in Fig. 8(f), it was thought that the density of Pt particle might have been too high and better to decrease to fabricate highly dispersed Pt loading sample. Because Pt can be loaded only on the surface and the sample used was not powder, the different measure than wt% was better to be used to quantify Pt content. Similarly, the surface area of Nb5 is much smaller than FN5, there is a possibility that Pt are not sufficiently dispersed on Nb5, which caused the insufficient reduction of Pt in Nb5. The quantification and optimization of Pt content will be of future study. It is expected that higher efficiency can be obtained by optimizing the amount of deposited Pt.

In this study, as a case study, we used photodeposition method to see the effect of cocatalyst. Since the advantage of the present method is the usage of dry processing, the photodeposition may deprive the original advantage. Thus, in future, it would be of interest to deposit cocatalyst using plasma, as was done in [65] using helicon sputtering device. The advantage of the prepared sample shown in this study is in fact that three dimensional porous nanostructures can be fabricated one step dry process. The bottom up process can tailor the nanostructures directly on the substrate and increase the effective surface area by an order of magnitude and the surface roughness in mesoporous scale. Comparison with samples prepared by conventional chemical processes will be of importance in future. Further analysis using other substrate than MB and characterization of prepared photocatalysts are of importance for future work.

6 Conclusions

In this study, systematic helium (He) plasma irradiation on niobium (Nb) substrate revealed that fiberform nanostructures (FNs) can be formed on Nb surface even though the shear modulus of Nb is rather low (~ 32 GPa). The growth mechanism was likely to be similar to the other metals where FNs can be formed by He plasma irradiation with the help of He bubble growth. Although growth of FNs on low shear modulus metals was thought to be difficult, this study revealed that FNs can be formed when we increase the He fluence higher than typically 3×10^{26} m⁻². FN growth was identified on Nb substrate when the surface temperature was in the range of 900-1100 K, and the incident ion energy was higher than ~ 70 eV.

The sample surface was oxidized at various temperatures, and formation of Nb₂O₅ was confirmed from the x-ray photoelectron spectroscopy analysis on all the sample surfaces at heating temperature up to 773 K. In addition to flat and FN Nb₂O₅ samples, we synthesized samples on which Pt nanoparticles were photodeposited. This was probably the first trial to conduct photodeposition

on plasma synthesized nanostructured substrate.

Photocatalytic performance was investigated using methylene blue (MB) decolorization experiments using ultra-violet (UV) irradiation. There was no significant difference between flat and FN samples with Pt deposition. Although the effective surface of the FN sample was greater than the flat sample, He plasma irradiation could have deteriorated the crystallinity, which consequently canceled out the benefit of FN samples. On the other hand, Pt deposition clearly enhanced the photocatalytic reactivity especially on FN samples. Photon absorbance was increased significantly in the wavelength range less than 400 nm from UV-VIS measurement, indicating that photo-excited electrons were produced efficiently on Pt deposited FN sample, which consequently contributed to decompose MB.

Acknowledgement

This work was supported in part by a Grant-in-Aid for Scientific Research (B) 15H04229, Grant-in-Aid for Exploratory Research 16K13917, Fund for the Promotion of Joint International Research 17KK0132 from the Japan Society for the Promotion of Science (JSPS), and JSPS Bilateral Joint Research Project. The authors thank Dr. M Tokitani and Mr D. Nagata from National Institute for Fusion Science (NIFS) for supporting TEM observations and Dr Y. Ichino from Nagoya University for supporting XRD measurement. .

References

- [1] R. A. Rani, A. S. Zoolfakar, J. Z. Ou, M. R. Field, M. Austin and K. Kalantar-zadeh: *Sensors and Actuators B: Chemical* **2013**, 176, 149.
- [2] M.-R. Ok, R. Ghosh, M. K. Brennaman, R. Lopez, T. J. Meyer and E. T. Samulski: *ACS Applied Materials & Interfaces* **2013**, 5, 3469, pMID: 23534849.
- [3] T. J. Novakowski, J. K. Tripathi and A. Hassanein: *ACS Applied Materials & Interfaces* **2016**, 8, 34896, pMID: 27998103.
- [4] M. Wei, K. Wei, M. Ichihara and H. Zhou: *Electrochemistry Communications* **2008**, 10, 980.
- [5] K. Nakajima, Y. Baba, R. Noma, M. Kitano, J. N. Kondo, S. Hayashi and M. Hara: *Journal of the American Chemical Society* **2011**, 133, 4224, pMID: 21370861.
- [6] H. Kominami, K. Oki, M. Kohno, S.-i. Onoue, Y. Kera and B. Ohtani: *J. Mater. Chem.* **2001**, 11, 604.
- [7] A. G. Prado, L. B. Bolzon, C. P. Pedroso, A. O. Moura and L. L. Costa: *Applied Catalysis B: Environmental* **2008**, 82, 219.

- [8] A. Fujishima and K. Honda: *Nature* **1972**, 238, 5358.
- [9] Z. Zou, J. Ye, K. Sayama and H. Arakawa: *nature* **2001**, 414, 625.
- [10] A. Kudo and Y. Miseki: *Chem. Soc. Rev.* **2009**, 38, 253.
- [11] X. Chen, T. Yu, X. Fan, H. Zhang, Z. Li, J. Ye and Z. Zou: *Applied Surface Science* **2007**, 253, 8500.
- [12] L. Li, J. Deng, R. Yu, J. Chen, Z. Wang and X. Xing: *J. Mater. Chem. A* **2013**, 1, 11894.
- [13] H. Zhang, Q. Lin, S. Ning, Y. Zhou, H. Lin, J. Long, Z. Zhang and X. Wang: *RSC Adv.* **2016**, 6, 96809.
- [14] S. Furukawa, Y. Ohno, T. Shishido, K. Teramura and T. Tanaka: *ACS Catalysis* **2011**, 1, 1150.
- [15] S. Qi, R. Zuo, Y. Liu and Y. Wang: *Materials Research Bulletin* **2013**, 48, 1213.
- [16] J. Xue, R. Wang, Z. Zhang and S. Qiu: *Dalton Trans.* **2016**, 45, 16519.
- [17] J. Bai, J. Xue, R. Wang, Z. Zhang and S. Qiu: *Dalton Trans.* **2018**, 47, 3400.
- [18] D. R. Rolison: *Science* **2003**, 299, 1698.
- [19] T. Sreethawong, S. Ngamsinlapasathian and S. Yoshikawa: *Materials Letters* **2012**, 78, 135.
- [20] S. Takamura, N. Ohno, D. Nishijima, and S. Kajita: *Plasma Fusion Res.* **2006**, 1, 051.
- [21] S. Takamura and Y. Uesugi: *Applied Surface Science* **2015**, 356, 888.
- [22] G. De Temmerman, K. Bystrov, J. J. Zielinski, M. Balden, G. Matern, C. Arnas and L. Marot: *Journal of Vacuum Science & Technology A* **2012**, 30, 041306.
- [23] P. Fiflis, M. Christenson, N. Connolly and D. Ruzic: *Nanomaterials* **2015**, 5, 2007.
- [24] K. Omori, A. M. Ito, K. Shiga, N. Yamashita, K. Ibano, H. T. Lee and Y. Ueda: *Journal of Applied Physics* **2017**, 121, 155301.
- [25] S. Kajita, T. Ishida, N. Ohno, D. Hwangbo and T. Yoshida: *Sci. Rep.* **2016**, 6, 30380.
- [26] S. Kajita, T. Nojima, Y. Tomita, N. Ohno, H. Tanaka, N. Yoshida, M. Yajima, T. Akiyama, M. Tokitani and T. Yagi: *Surface and Coatings Technology* **2018**, 340, 86.

- [27] I. Tanyeli, L. Marot, D. Mathys, M. C. M. van de Sanden and G. D. Temmerman: *Scientific Reports* **2015**, 5, 9779.
- [28] R. Farraro and R. B. McLellan: *Metallurgical Transactions A* **1979**, 10, 1699.
- [29] S. Kajita, T. Yoshida, D. Kitaoka, R. Etoh, M. Yajima, N. Ohno, H. Yoshida, N. Yoshida and Y. Terao: *Journal of Applied Physics* **2013**, 113, 134301.
- [30] M. de Respinis, G. De Temmerman, I. Tanyeli, M. C. van de Sanden, R. P. Doerner, M. J. Baldwin and R. van de Krol: *ACS Applied Materials & Interfaces* **2013**, 5, 7621.
- [31] K. Komori, T. Yoshida, T. Nomoto, M. Yamamoto, C. Tsukada, S. Yagi, M. Yajima, S. Kajita and N. Ohno: *Nuclear Instruments and Methods in Physics Research Section B: Beam Interactions with Materials and Atoms* **2015**, 365, Part A, 35 .
- [32] R. Sinha, I. Tanyeli, R. Lavrijsen, M. van de Sanden and A. Bieberle-Hutter: *Electrochimica Acta* **2017**, 258, 709.
- [33] A. Bieberle-Hutter, I. Tanyeli, R. Lavrijsen, B. Koopmans, R. Sinha and M. van de Sanden: *Thin Solid Films* **2017**, 631, 50.
- [34] S. Kajita, T. Yoshida, N. Ohno, T. Ishida and D. Kitaoka: *Japanese Journal of Applied Physics* **2016**, 55, 106202.
- [35] S. Kajita, T. Yoshida, N. Ohno, Y. Ichino and N. Yoshida: *Journal of Physics D: Applied Physics* **2018**, 51, 215201.
- [36] K. Maeda and K. Domen: *The Journal of Physical Chemistry Letters* **2010**, 1, 2655.
- [37] N. Ohno, D. Nishijima, S. Takamura, Y. Uesugi, M. Motoyama, N. Hattori, H. Arakawa, N. Ezumia, S. Krasheninnikov, A. Pigarov and U. Wenzel: *Nucl. Fusion* **2001**, 41, 1055.
- [38] S. Kajita, W. Sakaguchi, N. Ohno, N. Yoshida and T. Saeki: *Nucl. Fusion* **2009**, 49, 095005.
- [39] B. T. Barnes: *J. Opt. Soc. Am.* **1966**, 56, 1546.
- [40] J. M. Herrmann, J. Disdier and P. Pichat: *The Journal of Physical Chemistry* **1986**, 90, 6028.
- [41] X. Yan, T. Ohno, K. Nishijima, R. Abe and B. Ohtani: *Chemical Physics Letters* **2006**, 429, 606.
- [42] S. Kajita, A. M. Ito and N. Ohno: *Physics Letters A* **2017**, 381, 2355.

- [43] N. Ohno, Y. Hirahata, M. Yamagiwa, S. Kajita, M. Takagi, N. Yoshida, R. Yoshihara, T. Tokunaga and M. Tokitani: *Journal of Nuclear Materials* **2013**, 438, Supplement, S879.
- [44] S. Kajita, D. Kitaoka, N. Ohno, R. Yoshihara, N. Yoshida and T. Yoshida: *Applied Surface Science* **2014**, 303, 438.
- [45] S. Kajita, N. Yoshida, R. Yoshihara, N. Ohno and M. Yamagiwa: *J. Nucl. Mater.* **2011**, 418, 152.
- [46] D. Smith: *Journal of Nuclear Materials* **1978**, 75, 20.
- [47] W. Eckstein: *IPP* **2002**, 9/132.
- [48] T. Novakowski, J. Tripathi, G. Hosinski, G. Joseph and A. Hassanein: *Applied Surface Science* **2016**, 362, 35.
- [49] M. Yajima, N. Yoshida, S. Kajita, M. Tokitani, T. Baba and N. Ohno: *Journal of Nuclear Materials* **2014**, 449, 9.
- [50] Y. Noiri, S. Kajita and N. Ohno: *Journal of Nuclear Materials* **2015**, 463, 285.
- [51] M. Baldwin and R. Doerner: *Nucl. Fusion* **2008**, 48, 035001 (5pp).
- [52] R. Smirnov and S. Krasheninnikov: *Nuclear Fusion* **2013**, 53, 082002.
- [53] S. Kajita, S. Kawaguchi, N. Ohno and N. Yoshida: *Scientific reports* **2018**, 8, 56.
- [54] *Landolt-Bornstein Numerical Data and Functional Relationships in Science and Technology Group III* (Springer, Heidelberg, 1985), Vol. 15.
- [55] S. Kajita, T. Saeki, N. Yoshida, N. Ohno and A. Iwamae: *Applied Physics Express* **2010**, 3, 085204.
- [56] F. Amano, K. Nogami, M. Tanaka and B. Ohtani: *Langmuir* **2010**, 26, 7174.
- [57] M. Yajima, Y. Hatano, S. Kajita, J. Shi, M. Hara and N. Ohno: *Journal of Nuclear Materials* **2013**, 438, S1142.
- [58] O. D. Coskun, S. Demirel and G. Atak: *Journal of Alloys and Compounds* **2015**, 648, 994.
- [59] J.-J. Shao, Z.-J. Li, C. Zhang, L.-F. Zhang and Q.-H. Yang: *J. Mater. Chem. A* **2014**, 2, 1940.
- [60] S. Kajita, N. Yoshida, N. Ohno and Y. Tsuji: *New Journal of Physics* **2015**, 17, 043038.
- [61] J. Liu, D. Xue and K. Li: *Nanoscale Research Letters* **2011**, 6, 138.

- [62] R. Sakamoto, E. Bernard, A. Kreter and N. Yoshida: *Nuclear Fusion* **2017**, 57, 016040.
- [63] N. Shinada: *Journal of the Japan Society of Colour Material* **1969**, 42, 470.
- [64] C. Langhammer, Z. Yuan, I. Zoric and B. Kasemo: *Nano Letters* **2006**, 6, 833, pMID: 16608293.
- [65] Y. Zhong, K. Ueno, Y. Mori, T. Oshikiri and H. Misawa: *The Journal of Physical Chemistry C* **2015**, 119, 8889.

Table 1: Summary of samples used for photocatalysts.

| Sample | Surface | Oxidization | Loading |
|--------|---------|-------------|---------|
| Nb1 | flat | RT | – |
| Nb2 | flat | 573 K | – |
| Nb3 | flat | 673 K | – |
| Nb4 | flat | 773 K | – |
| Nb5 | flat | 773 K | Pt |
| FN1 | FNs | RT | – |
| FN2 | FNs | 573 K | – |
| FN3 | FNs | 673 K | – |
| FN4 | FNs | 773 K | – |
| FN5 | FNs | 773 K | Pt |

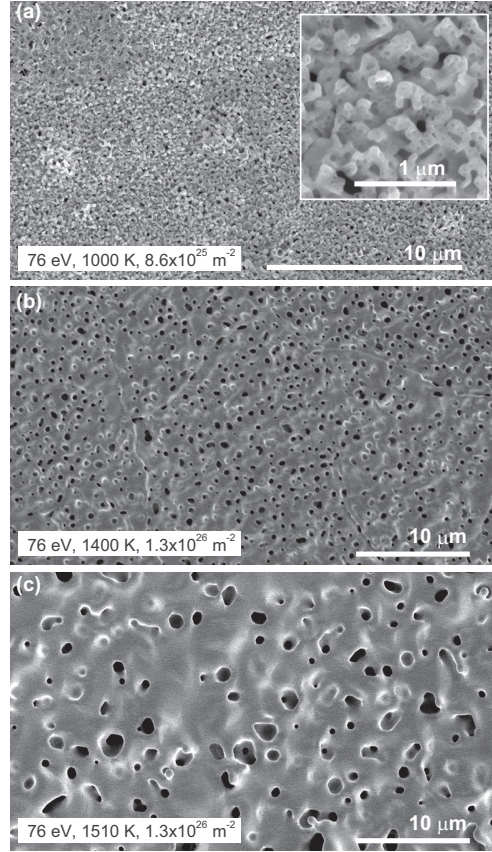


Figure 1: SEM micrographs of Nb surfaces exposed to He plasmas at T_s of (a) 1000, (b) 1400, and (c) 1510 K; E_i was 76 eV, and Φ_{He} , was in the range of $8.6\text{-}13 \times 10^{25} \text{ m}^{-2}$.

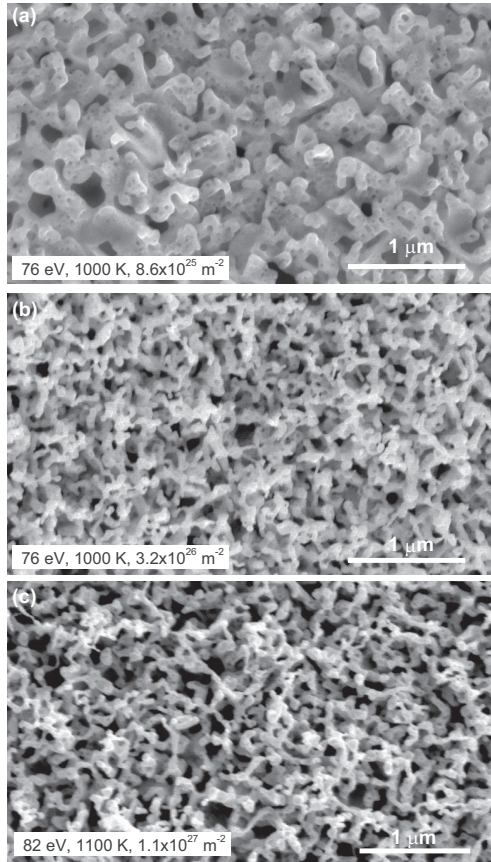


Figure 2: He fluence dependence of the morphology change; T_s was (a,b) 1000 and (c) 1100 K, and E_i was (a,b) 76 and (c) 82 eV. The irradiation time was (a) 1, (b) 3, and (c) 10 h.

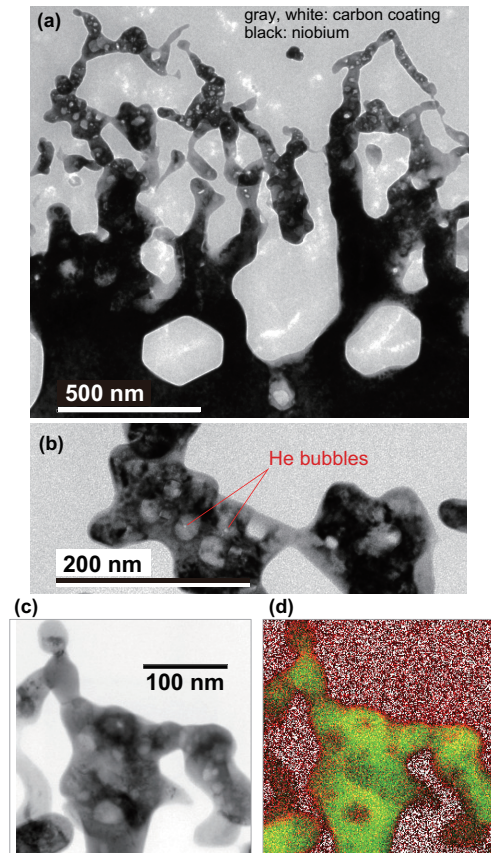


Figure 3: (a,b) TEM micrographs of an FN sample at different magnifications. The irradiation condition of the sample was as follows: T_s was 1100 K, E_i was 82 eV, and Φ_{He} was $\sim 4 \times 10^{26} \text{ m}^{-2}$. (c) is a TEM micrograph of an FN sample, and (d) shows a color mapping of the area shown in (c) (green:Nb, red:oxygen).

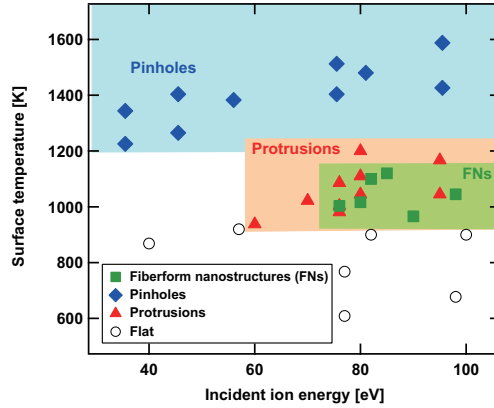


Figure 4: Summary of the relationship between the irradiation condition (T_s and E_i) and morphology changes. The irradiations time was 1h (flat, pinholes, protrusions) or 3h (FNs). Morphology changes were categorized for different ones: no changes (flat), pinholes, protrusions, and FNs.

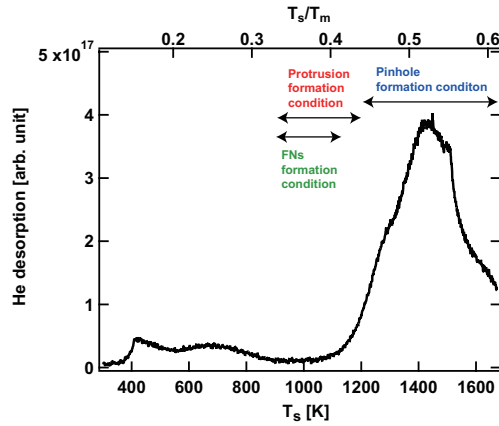


Figure 5: A thermal desorption spectroscopy (TDS) spectrum of the sample with FNs. For reference, temperature windows for three typical morphology changes, i.e., FN, protrusion, pinhole, are presented.

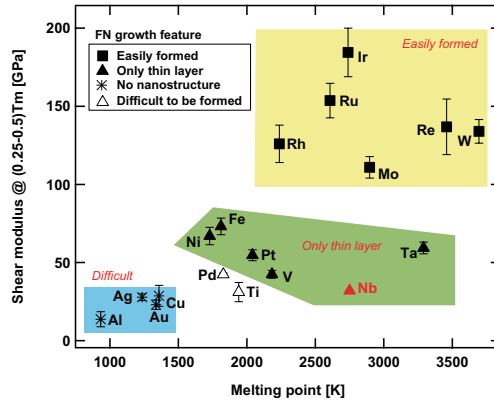


Figure 6: FN growth features on various metals plotted with different markers in terms of the melting point, T_m , and the shear modulus. The shear modulus was the averaged value between $0.25T_m$ and $0.5T_m$, and the error bars represent the minimum and maximum values in the temperature region.

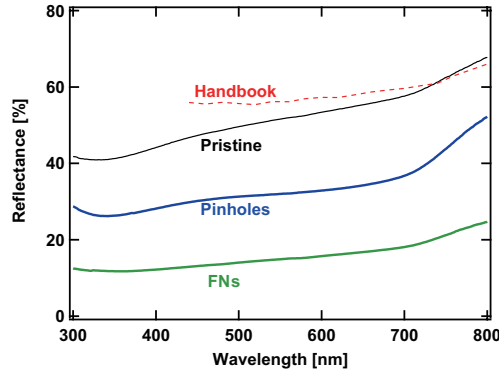


Figure 7: The wavelength dependence of the reflectance of a pristine, pinhole, and FN samples together with a handbook value [54].

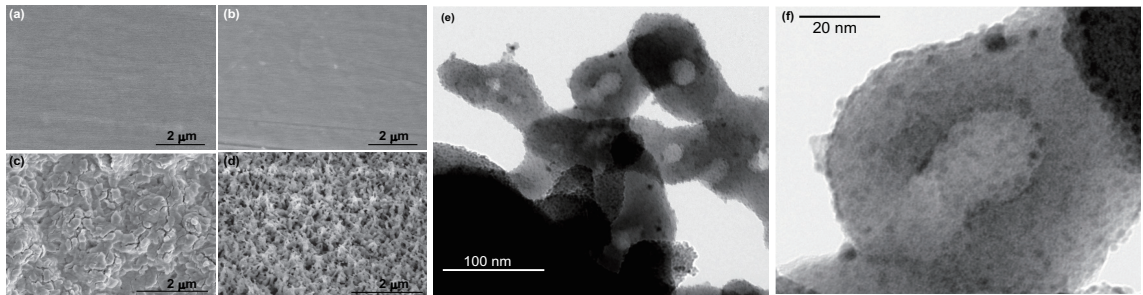


Figure 8: SEM micrographs of (a) Nb2, (b) Nb3, (c) Nb4, and (d) FN4, and (e,f) TEM micrographs of Pt-FN sample.

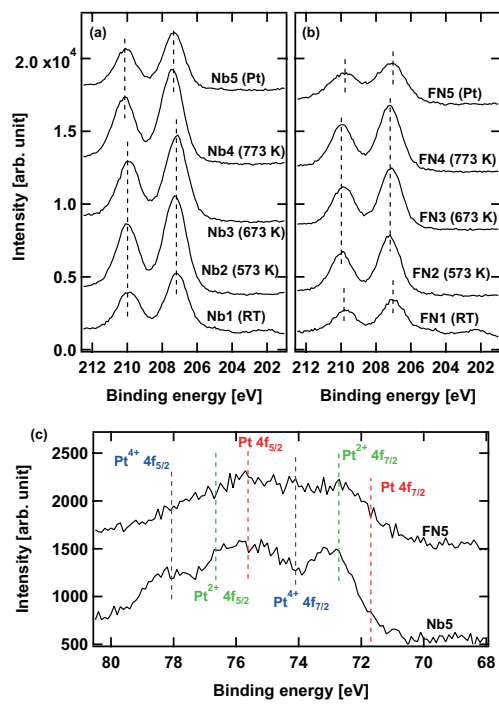


Figure 9: Nb 3d photoelectron spectra of (a) Nb1-Nb5 and (b) FN1-FN5, and (c) Pt 4f photoelectron spectra of Nb5 and FN5.

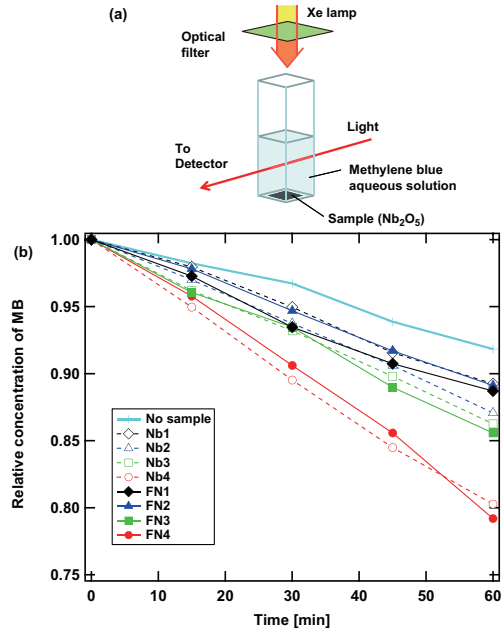


Figure 10: (a) A schematic of the MB experiments and (b) time courses of MB concentration during UV light irradiation on Nb1-4 and FN1-4 samples together with the case without any sample (control).

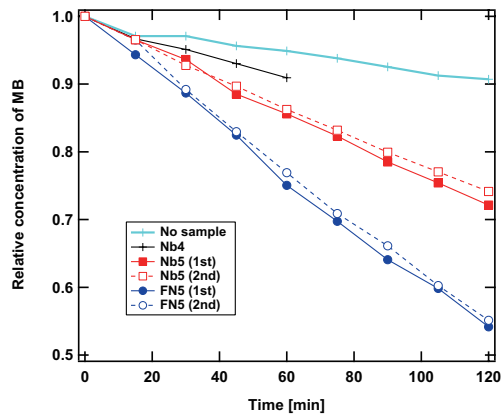


Figure 11: Time courses of MB concentration during UV light irradiation on Nb5 and FN5. The case without any sample (control) and Nb4 case were also presented. Dotted lines represent the recycle performance of Nb5 and FN5.

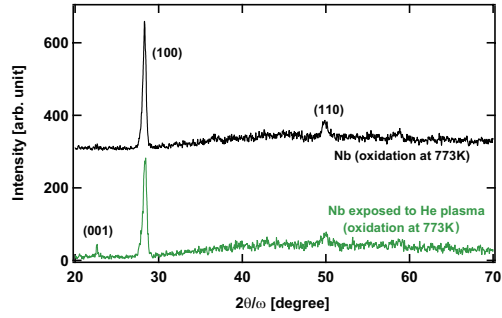


Figure 12: XRD patterns of the oxidized Nb samples at 773 K before and after He plasma irradiation.

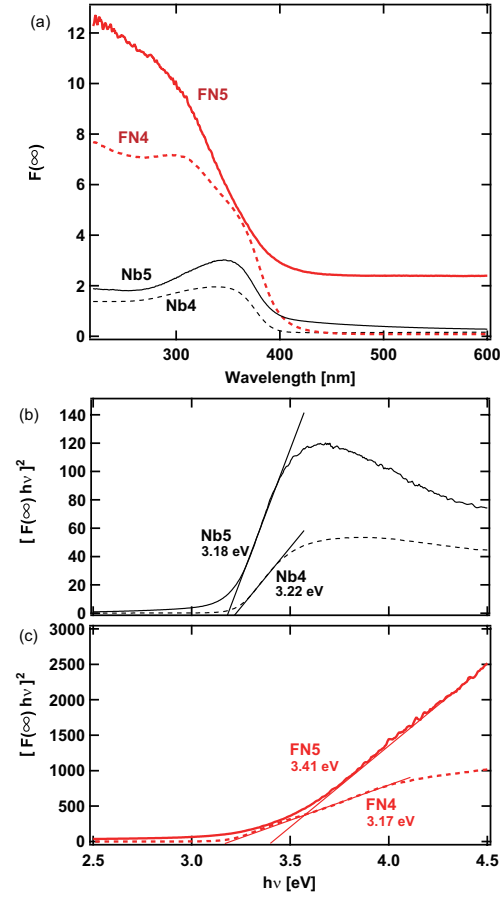


Figure 13: (a) UV-visible diffuse reflectance spectra of Nb4, Nb5, FN4, and FN5 and (b,c) Kubelka-Munk plots of Nb4,5 and FN4,5, respectively.